12C.1   MINI-SUPERCELLS OBSERVED IN AN OFFSHORE OUTER RAINBAND OF HURRICANE IVAN (2004)

Matthew D. Eastin*
M. Christopher Link

Department of Geography and Earth Sciences,
University of North Carolina at Charlotte, Charlotte, North Carolina

1. INTRODUCTION

The majority of landfalling tropical cyclones produce tornadoes. In the United States, as much as 10% of all deaths associated with tropical cyclones (TCs) are the result of tornadoes (Novlan and Gray 1974). To date, forecasting such TC tornado events remains a significant challenge since the typical TC environment is often very different from the typical tornadic environment.

A number of observational and numerical studies have documented common environmental and storm-scale characteristics associated with the formation of TC tornadoes (Novlan and Gray 1974; Gentry 1983; McCaul 1991; McCaul and Weisman 1996; Spratt et al. 2000; McCaul et al. 2004; Curtis 2004; Schneider and Sharp 2007). TC tornadoes predominantly form in convective outer rainbands located in the onshore flow of the right-front quadrant, usually within 100 to 400 km of the storm center. Favorable environmental characteristics include: strong low-level shear (> 20 m/s over the lowest 3 km), moderate CAPE (> 500 J/kg), strong low-level storm-relative helicity (> 100 m^2/s^2), dry air at midlevels adjacent to the rainband, a low-level thermal boundary or convergence axis, and small near-surface dewpoint depressions (i.e., a low LCL). Many TC tornadoes are spawned by "mini-supercells", which are shallower (echo tops < 8-12 km) and smaller in diameter (< 10 km) than the classic Great Plains supercells. On radar, mini-supercells often exhibit weak hook echoes and shallow (< 5 km), small diameter (< 4 km) mesocyclones with storm-relative rotational velocities of 5-20 m/s. The mesocyclones are often short lived (< 20 min) but detectable 10-15 min prior to tornadogenesis.

Based on a review of previous studies, the current working model for TC tornadogenesis embodies a two-stage process that begins as convective cells (e.g. within an outer rainband) move onshore. During this transition from the offshore regime, en-hanced surface friction increases the low-level shear and storm-relative helicity such that the local low-CAPE environment becomes favorable for the formation of mini-supercells (McCaul and Weisman 1996). Tornadogenesis is then believed to result from the tilting and subsequent stretching of this shear-generated horizontal vorticity into the vertical by buoyant updrafts (Gentry 1983). Further enhancements to the local horizontal vorticity (and the increased likelihood of tornadogenesis) can result as the cell moves over and/or interacts with pre-existing thermal boundaries, convergence zones, or outflow boundaries (generated by evaporatively-driven downdrafts). Indeed, the majority of TC mesocyclones are first observed as the cells move onshore, and many TC tornadoes are reported within 300 km of the coast during short-lived interactions with low-level boundaries.

There are also a considerable number of TC tornadoes that are reported within 10 km of the coastline. Such cases may represent an accelerated version of the conceptual model, whereby the supercell development and tornadogenesis processes simply occur over a much shorter time period (and distance) due to a very rapid increases in vertical shear and low-level convergence. However, *another possible explanation is that the mini-supercells developed well offshore.* Indeed, Bogner at al. (2000) demonstrated that the offshore TC environment is often conducive to supercell formation. Unfortunately, observations and statistics of offshore development from land-based radars are limited due to sampling considerations (Spratt et al. 2000).

The objectives of this study are to document the three-dimensional structure and evolution of *offshore* mini-supercells embedded within an outer rainband of Hurricane Ivan (2004). To achieve this goal, we employ an array of land-based and airborne observations. We will demonstrate that (1) the mesoscale environment of the rainband was conducive to supercell formation, (2) three distinct mini-supercells were present as far as 150 km offshore, (3) tilting and subsequent stretching of low-level horizontal vorticity by the updrafts contributed to mesocyclone formation, and (4) one of these mini-supercells produced deadly tornadoes soon after moving onshore.

* *Corresponding Author Address:* Matthew D. Eastin, Department of Geography and Earth Sciences, University of North Carolina at Charlotte, 9201 University City Blvd, Charlotte, NC 28223; email: mdeastin@uncc.edu,

2. DATA AND MESOSCALE OVERVIEW

Hurricane Ivan made landfall early on 16 September 2004 just west of Gulf Shores, Alabama as a category 3 hurricane. Over 115 tornadoes were reported as Ivan crossed the southeast United States. Eight people were killed and 17 were injured by the tornadoes. The most significant tornadic activity occurred during the afternoon and evening of 15 September as Ivan approached the Gulf coast. During this time, an intense outer rainband developed ~400 km east of the storm center and produced multiple supercells over the Florida panhandle (see Figs. 1 and 2). This paper examines a subset of these supercells.

During the afternoon and evening of 15 September, NOAA research aircraft observed Ivan's offshore environment and inner core. A WP-3D aircraft crossed the intense outer rainband (see Figs. 1, 2, and 5) as they ferried between Ivan's eyewall and MacDill Air Force Base in Tampa, Florida. (The primary goals of the research missions were not to document the rainband, but rather the eyewall structure and evolution at landfall.) The aircraft employed the the fore-aft scanning technique (FAST) to collect dual-Doppler velocity data within the rainband during the pass (discussed in the next section). The G-IV aircraft flew around Ivan deploying multiple GPS dropwindsondes in the offshore rainband environment. Conventional satellite, rawindsonde, and the WSR-88D radar data from Tampa (TBW) and Tallahassee (TLH) were also incorporated to provide more complete depiction of the rainband environment and convective cell evolution.

Our period of interest encompasses 1500-2100 UTC on 15 September. Figure 1a shows the 89-GHz ice-scattering signature within Hurricane Ivan at 1850 UTC. The outer rainband is oriented along a south-north line and contains multiple deep convective cells (low brightness temperatures). Animated GOES-IR imagery (not shown) suggests that these cells comprise a series of convective bursts whereby cells first develop along the southern end and move northward. Figure 2 shows the base reflectivity field from the TLH and TBW radars at 1800 UTC. Multiple deep convective cells are oriented along a southeast-northwest line at regular 20-40 km intervals. Note that many cells (as viewed from TLH) within 20-50 km of the coastline (150-180 km from the radar) exhibit hook-like appendages indicative of supercells, but few cells at greater distances exhibit such structure. The stratiform rain shield extends to the east and northeast away from the TC center, whereas the western (inner) edge is characterized by strong reflectivity gradients and minimal stratiform precipitation. Figure 1b shows the GOES water va-

por signature from 1825 UTC. A distinct slot of midlevel dry air is located just west of the rainband.

At 1800 UTC the thermodynamic sounding from Tampa Bay (Fig. 3; ~200 km east of the rainband) revealed a shallow moist layer near the surface (below 900 mb), drier air at midlevels (900-400 mb), and moist air aloft (above 400 mb). Conditional instability (for a surface parcel) was present through a deep layer with a CAPE of ~2500 J/kg. The vertical wind profile exhibits modest shear (13-14 m/s) and storm-relative helicity (~ 75 m^2/s^2) over the 0-3 km layer. The thermodynamic sounding from the GPS dropsonde deployed at 1807 UTC (Fig. 4; ~40 km west of the rainband) revealed cooler and drier air near the surface, less conditional instability (CAPE ~700 J/kg) that was restricted to mid-levels (800-400 mb), and a stable layer aloft. In contrast, the vertical wind profile exhibits strong shear (20-22 m/s) and high storm-relative helicity (~ 180 m^2/s^2) over the lower levels. Both soundings support the potential for deep, rotating convection.

3. CONVECTIVE CELL STRUCTURE

Here we present the dual-Doppler observations collected between 1754 and 1810 UTC as an WP-3D aircraft passed through the rainband at 2.5 km altitude (see the black rectangles in Fig. 2). The three-dimensional wind field was constructed following the methods of Gamache (1997). During this period, the observed cells were located ~150 km offshore, and the mean cell motion was at 23 m/s from the south-southeast (i.e., the cells were moving ~10 m/s slower than the deep-layer mean wind).

Shown in Figure 5 are the radar reflectivity and storm-relative winds at 1.5 km altitude from the dual-Doppler analysis. Three distinct cells (labeled A, B, and C) are evident. Moreover, each cell contains modest cyclonic rotation in the storm-relative wind field (i.e., a mesocyclone) and a hook-like reflectivity appendage. Further examination reveals that each mesocyclone is also roughly collocated with the updraft and vertical vorticity maxima of their host cell (see Fig. 6). Clearly, each cell contains a rotating updraft: the signature of a supercell.

Figures 7 and 8 show an east-west and north-south cross-section, respectively through the center of Cell B (see Fig. 6 for orientation). The mesocyclone (arbitrarily defined by the 2 x 10^{-3} s^{-1} vertical vorticity contour) extends from near the surface up to ~4 km altitude with a diameter of ~5-6 km. The primary low-level updraft (located at x = 30 km, y = 36 km, and defined by the 2 m/s vertical velocity contour) extends from ~1.0 km upward to ~4.5 km with a similar diameter. Such dimensions are consistent with previous observations of *mini-supercells* within tropical cyclones (Spratt et

al. 1997; McCaul et al. 2004; Schneider and Sharp 2007). Furthermore, note how the vorticity maximum ($\sim$9 x 10^{-3} s^{-1} at 1 km altitude) is located below the updraft maximum ($\sim$6 m/s at 2.5 km altitude), which suggests that vorticity stretching by the updraft may further enhance the low-level vorticity maximum. The primary updraft tilts to the northeast with height in a manner consistent with the local environmental shear vector (see Figs 3 and 4). Modest midlevel downdrafts are located to the southwest and northeast of the primary updraft but do not penetrate below 1 km altitude. Their locations are roughly consistent with the rear-flank and forward flank downdrafts, respectively, that are commonly observed in Great Plains supercells. Cross-sections through Cells A and C (not shown) exhibit similar structure.

4. **VERTICAL VORTICITY BUDGET**

The mechanism for vertical vorticity production at mid-levels in mini-supercells is believed to be the tilting of horizontal vorticity (induced by low-level strong vertical shear) into the vertical and its subsequent stretching by an updraft that intensifies with height (Rotunno 1981; McCaul and Weisman 1996). Low-level vertical vorticity production is believed to result from either the vertical tilting of baroclinically or shear generated horizontal vorticity as it comes into contact with a strong updraft (e.g. Rotunno and Klemp 1983; Davies-Jones 1984) or through the stretching of ambient vertical vorticity by local updrafts along a convergence line (e.g. Roberts and Wilson 1995). In order to gain a better understanding of the mechanisms responsible for the formation and maintenance of the shallow mesocyclones, we examined the dual-Doppler derived low-level horizontal vorticity structure and a vertical vorticity budget in the vicinity of each cell.

Figures 9 and 10 show the horizontal vorticity vectors and magnitude at 1 km altitude near Cell B. Trajectory analysis (not shown) suggests that air entering the mesocyclone/updraft base approached from the east-southeast. In this region, a strong correlation between the horizontal vorticity and cell-relative wind vectors is apparent (see Fig. 9), implying the tilting of low-level streamwise vorticity by the cell's updraft largely contributed to development of the low-level mesocyclone. Note that the orientation of the horizontal vorticity vector is consistent with the vertical shear profile (i.e. clockwise turning hodographs) observed by the two soundings (see Figs 3 and 4). Baroclinic contributions, however, are difficult to assess due to the limited surface observations. Furthermore, comparisons between Figs. 6, 7, 8, and 10 suggests that the peak ambient horizontal vorticity and mesocyclonic vertical vorticity are of similar magnitudes ($\sim$10 x 10^{-3} s^{-1}).

Neglecting contributions from the Coriolis parameter and the solenoidal term, the generation of the vertical vorticity is can be defined as the sum of advective (both vertical and horizontal), stretching, and tilting terms (see Roberts and Wilson 1995). Shown in Figure 11 are the vertical vorticity generation and its production terms at 1 km altitude in the vicinity of Cell B. Both the primary mesocyclonic updraft (at 30,36 km) and a secondary updraft (at 36,36 km) contained net cyclonic vorticity production (Fig. 11a). For the primary mesocyclone, the dominant source was the stretching of pre-existing vertical vorticity (Fig. 11c) by the accelerating updraft (see Fig. 7), while the tilting of horizontal vorticity (Fig. 11d) also made a positive contribution on its eastern flank. The advective contribution at this altitude was largely negative due to the vertical advection imposed by the updraft. In contrast, the secondary updraft received roughly equal contributions from the stretching and tilting terms. It is interesting to note that the large advective production on its western flank results primary from horizontal contributions. Such westward advection of this secondary vertical vorticity maximum may contribute to the development and maintenance of the primary mesocyclone through local merger events.

The low-level horizontal vorticity and vertical vorticity budget terms in the vicinity of Cells A and C (not shown) depict a qualitatively consistent scenario for mesocyclone development.

5. **COASTLINE TORNADOGENESIS**

Using the Tallahassee (TLH) radar, the three mini-supercells were tracked from their offshore location at $\sim$1804 UTC until $\sim$2100 UTC (Figure 12a), by which time each cell had moved onshore along the Florida panhandle.

From the TLH perspective, Cells A and B first exhibited a prominent hook echo when they were located $\sim$25 km offshore and $\sim$140 km from the radar. The hook echoes persisted for $\sim$30-40 minutes as the cells paralleled the coast ($\sim$15 km offshore and $\sim$130 km from the radar), but became less distinct as the cells moved onshore (see Fig. 8). No tornadoes nor radar-detected mesocyclones were observed in association with Cell A during this period. A weak mesocyclone was briefly detected within Cell B (at 1945 UTC) as it was located over a barrier island south of Panama City Beach ($<$ 10 km offshore and $\sim$125 km from the radar), but no tornadoes were reported.

Cell C first exhibited a hook echo at 1934 UTC when it was located $\sim$32 km offshore and $\sim$140 km from the radar. The hook echo persisted over the next 90 minutes as the cell paralleled the coast and

then moved onshore south of Panama City Beach. A weak to moderate mesocyclone was detected by the TLH radar between 2022 and 2040 UTC as the cell moved from ∼10 km offshore to ∼5 km onshore (at ∼120-130 km from the radar). Cell C spawned up to three tornadoes between 2040 and 2055 UTC: the most intense killed one person and injured seven others as it produced F1 damage moving through a commercial district.

6. DISCUSSION

Our results from Hurricane Ivan indicate that mini-supercells can indeed develop more than 150 km offshore within the tropical cyclone outer rainband environment. The cells exhibited many of the same structural characteristics as the mini-supercells often observed moving onshore or well inland. The high-resolution dual-Doppler analysis revealed that the tilting of low-level horizontal (streamwise) vorticity (generated by vertical shear) into the vertical and subsequent stretching by an accelerating updraft appears to have been largely responsible for the mesocyclone formations. Contributions from baroclinic forces and local merger events may also contribute. Whether these cells maintained their supercellular structure during the 2-3 hour period prior to landfall and tornadogenesis is unclear, but the detection of mesocyclones by land-based radars when the cells were still offshore is suggestive of such evolution. It is also possible the cells underwent cyclic mesocyclonegensis (e.g. Alderman et al. 1999). Furthermore, the extent to which the convective structures observed within Ivan's offshore rainband are typical remains an open question. Indeed, many environmental characteristics conducive to supercell formation (e.g. large CAPE, large low-level storm-relative helicity, and a midlevel dry air intrusion) were not only present, but greater in magnitude than normal (McCaul 1991; Bogner et al. 2000).

The early identification and regular monitoring of mini-supercells is crucial to operational forecasting. Unfortunately, the detection of mini-supercells at large ranges from land-based radars (i.e., far offshore) can be limited due to the cell's diminutive structure and radar sampling considerations (Spratt et al. 1997). For example, Cell B was located ∼220 km away from the Tallahassee radar when the dual-Doppler analysis was performed. At this range, the 0.5° beam passes through the cell at ∼5 km altitude and effectively overshoots the shallow mesocyclone and its associated low-level reflectivity structure. Thus, in an attempt to extend our ability to monitor offshore supercells, ongoing research also involves documenting the radar characteristics of numerous tornadic and non-tornadic cells as they move onshore, as well as the radar characteristics of those offshore mini-supercells identified by the airborne dual-Doppler analyses.

REFERENCES

Adlerman, E. J., K. K. Droegemeier, and R. Davies-Jones, 1999: A numerical simulation of cyclic mesocyclogensis. *J. Atmos. Sci.*, **56**, 2045-2069.

Bogner, P. B., G. M. Barnes, and J. L. Franklin, 2000: Conditional instability and shear for six hurricanes over the Atlantic Ocean. *Wea. Forecasting*, **15**, 192-207.

Curtis, L., 2004: Midlevel dry intrusions as a factor in tornado outbreaks associated with landfalling tropical cyclones for the Atlantic and Gulf of Mexico. *Wea. Forecasting*, **19**, 411-427.

Davies-Jones, R., 1984: Streamwise vorticity: The origin of updraft rotation in supercell storms. *J. Atmos. Sci.*, **41**, 2991-3006.

Gamache, J. F., 1997: Evaluation of a fully three-dimensional variational Doppler analysis technique. Preprints, *28th Conf. on Radar Meteorology*, Austin, TX, Amer. Meteor. Soc., 422-423.

Gentry, R. C. , 1983: Genesis of tornadoes associated with hurricanes, *Mon. Wea. Rev.*, **115**, 1793-1805.

Klemp, J. B., and R. Rotunno, 1983: A study of the tornadic region within a supercell thunderstorm. *J. Atmos. Sci.*, **40**, 359-377.

McCaul, E. W., Jr, 1991:Buoyancy and shear characteristics of hurricane-tornado environments. *Mon. Wea. Rev.*, **119**, 1954-1978.

McCaul, E. W., Jr., D. E. Buechler, S. J. Goodman, and M. Cammarata, 2004: Doppler radar and lightning network observations of a severe outbreak of tropical cyclone tornadoes. *Mon. Wea. Rev.*, **132**, 1747-1763.

McCaul, E. W., and M. L. Weisman, 1996: Simulations of shallow supercells in landfalling hurricane environments. *Mon. Wea. Rev.*, **124**, 408-429.

Novlan, D. J., and W. M. Gray, 1974: Hurricane-spawned tornadoes. *Mon. Wea. Rev.*, **102**, 476-488.

Roberts, R., and J. Wilson, 1995: The genesis of three nonsupercell tornadoes observed with dual-Doppler radar. *Mon. Wea. Rev.*, **123**, 3408-3436.

Rotunno, R., 1981: On the evolution of thunderstorm rotation. *Mon. Wea. Rev.*, **109**, 577-586.

Schneider, D., and S. Sharp, 2007: Radar signatures of tropical cyclone tornadoes in central North Carolina. *Wea. Forecasting*, **22**, 479-501.

Spratt, S. M., D. W. Sharp, P. Welsh, A. Sandrik, F. Alsheimer, and C. Paxton, 1997: A WSR-88D assessment of tropical cyclone outer rainband tornadoes. *Wea. Forecasting*, **13**, 479-501.
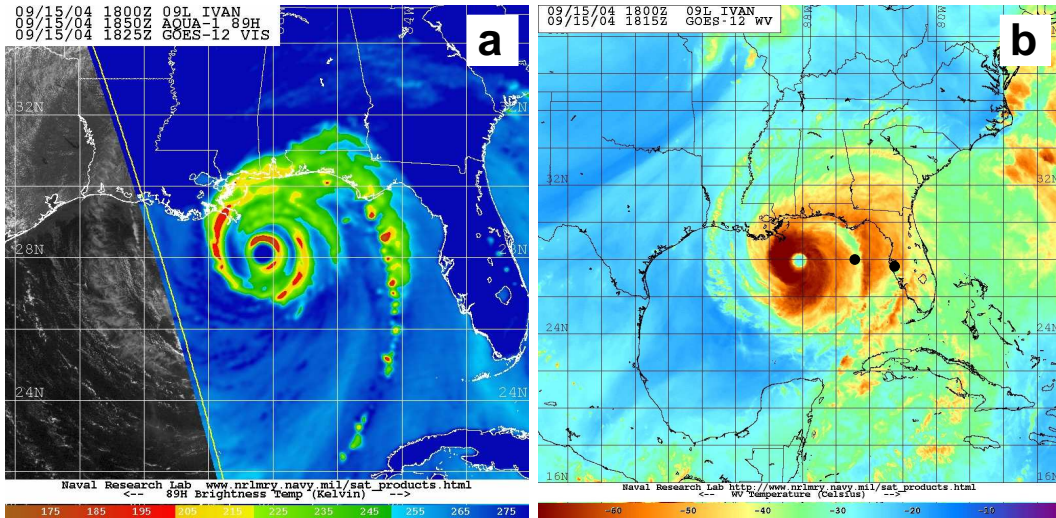
Figure 1: (a) 89-GHz brightness temperatures at 1850 UTC and (b) water vapor temperatures at 1815 UTC in Hurricane Ivan on 15 September 2004. Note the intense convective cells embedded within the outer rainband east of the storm center, as well as the dry air intrusion between the moist outer rainband and the inner core. Black dots in (b) denote the locations of representative soundings. Images from the NRL Tropical Cyclone Page.
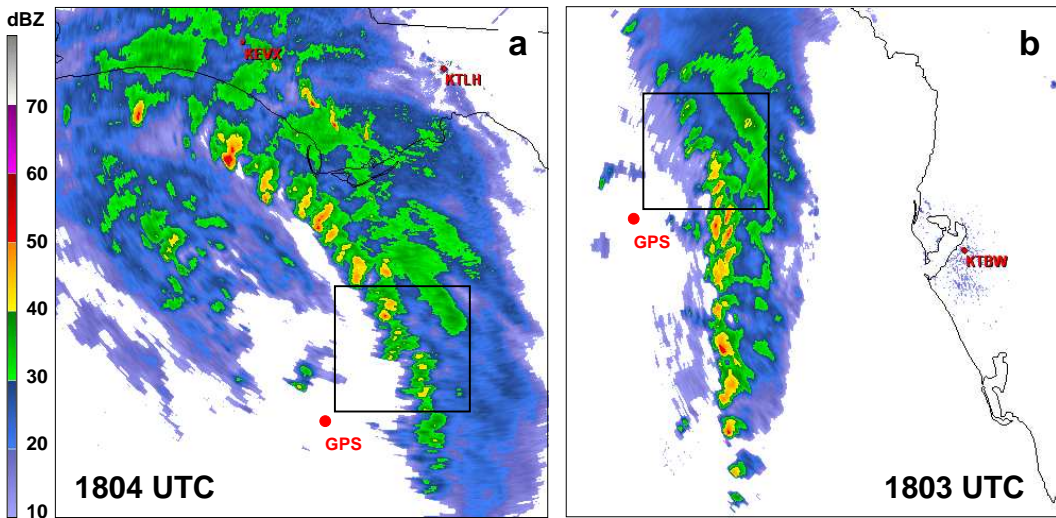

Figure 2: Base scan radar reflectivity (in dBZ) from (a) Tallahassee, FL (TLH) at 1804 UTC and (b) Tampa, FL (TBW) at 1803 UTC on 15 September 2004. The location of the dual-Doppler analysis region is shown with a black square. The location of the GPS dropsonde deployed at 1807 UTC is also shown.
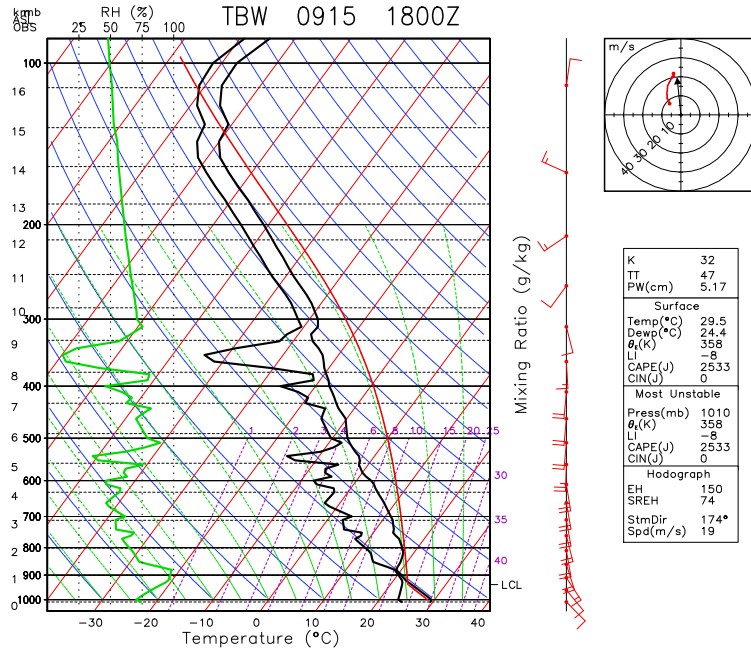
Figure 3: Skew-T plot of temperature, dewpoint, relative humidity, and winds for the Tampa sounding at 1800 UTC on 15 September 2004. Also shown is a surface-based parcel (red), the SFC-700 mb hodograph, an estimated cell motion vector (from the 900-200 mb mean wind), and a selection of standard stability and vertical shear indices.
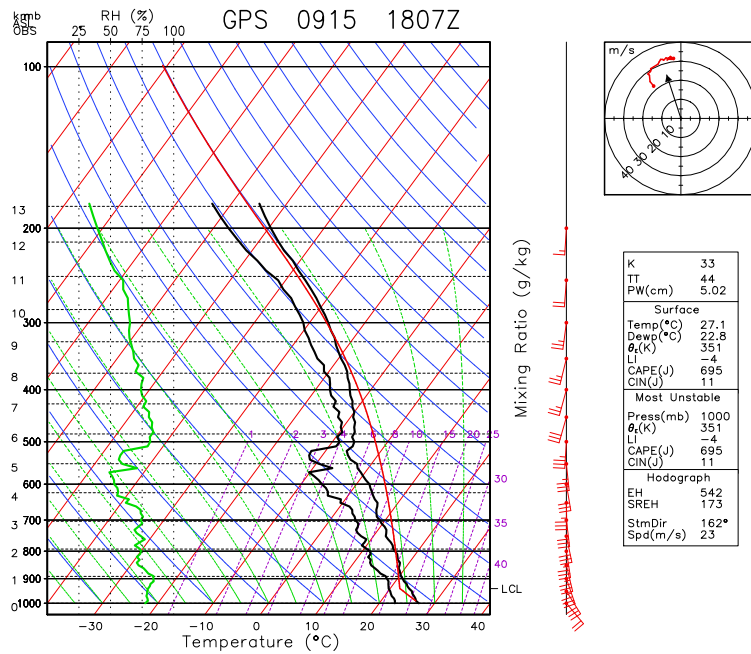
Figure 4: As in Figure 3, but for the GPS dropsonde deployed at 1807 UTC west of the rainband. The observed cell motion was used rather than an estimate from the deep layer mean wind.
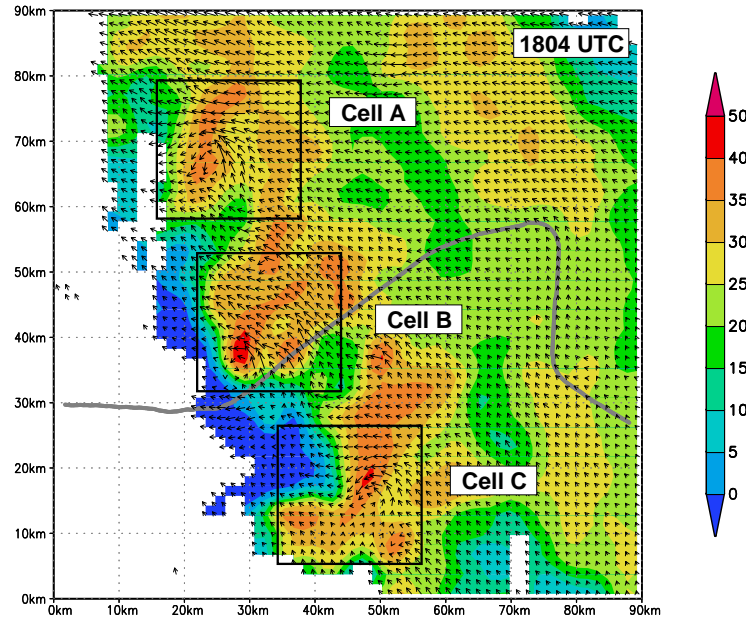
Figure 5: Radar reflectivity (color shading) and dual-Doppler derived cell-relative wind vectors at 1.5 km altitude at ∼1804 UTC on 15 September 2004. Also shown is the NOAA WP-3D flight track between 1754 and 1810 UTC (gray line). Note the mesocyclonic flow associated with each cell.
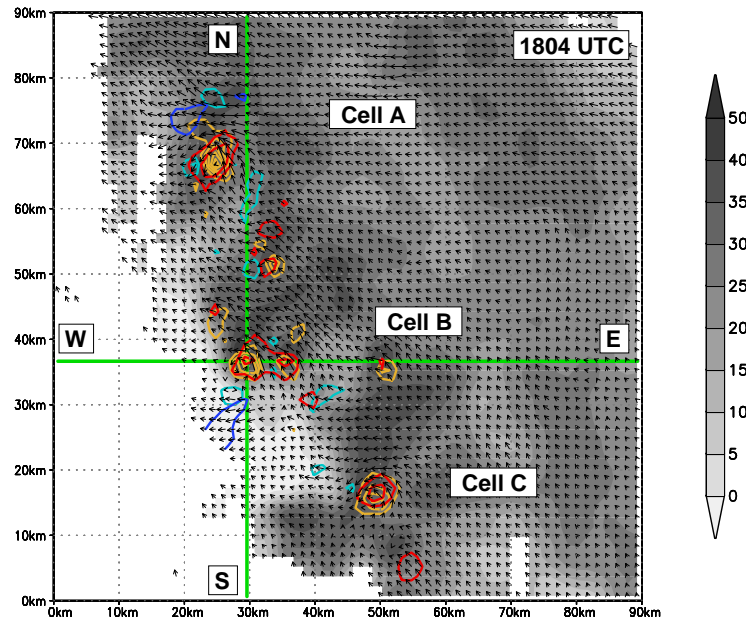
Figure 6: Radar reflectivity (gray-scale shading), vertical velocity $> \pm 2$ m s^{-1} (updrafts (downdrafts) are shown using red (blue) contours), vertical vorticity $> \pm 2$ x 10^{-3} s^{-1} (cyclonic (anticyclonic) are shown using orange (cyan) contours), and cell-relative wind vectors at 1.5 km altitude. Contour intervals of ± 2 m s^{-1} and ± 2 x 10^{-3} s^{-1} are used for vertical velocity and vertical vorticity, respectively. Green lines denote the locations of cross-sections shown in Figures 7 and 8. Note the collocated updraft and vorticity maxima; the defining signature of a rotating updraft within a supercell.
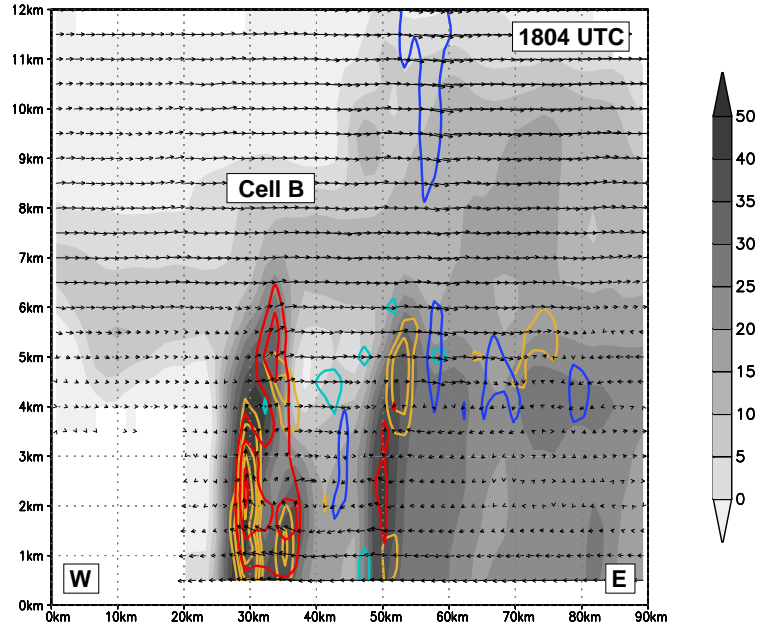
Figure 7: Radar reflectivity (gray-scale shading), vertical velocity $> \pm 2 \text{ m s}^{-1}$ (updrafts (downdrafts) are shown using red (blue) contours) and vertical vorticity $> \pm 2 \text{ x } 10^{-3} \text{ s}^{-1}$ (cyclonic (anticyclonic) are shown using orange (cyan) contours) along an east-west cross-section through Cell B. Contour intervals of $\pm 2 \text{ m s}^{-1}$ and $\pm 2 \text{ x } 10^{-3} \text{ s}^{-1}$ are used for vertical velocity and vertical vorticity, respectively. Wind vectors depict the vertical and cell-relative zonal flow. Note the cyclonic vorticity maxima located below each updraft maxima associated with Cell B.
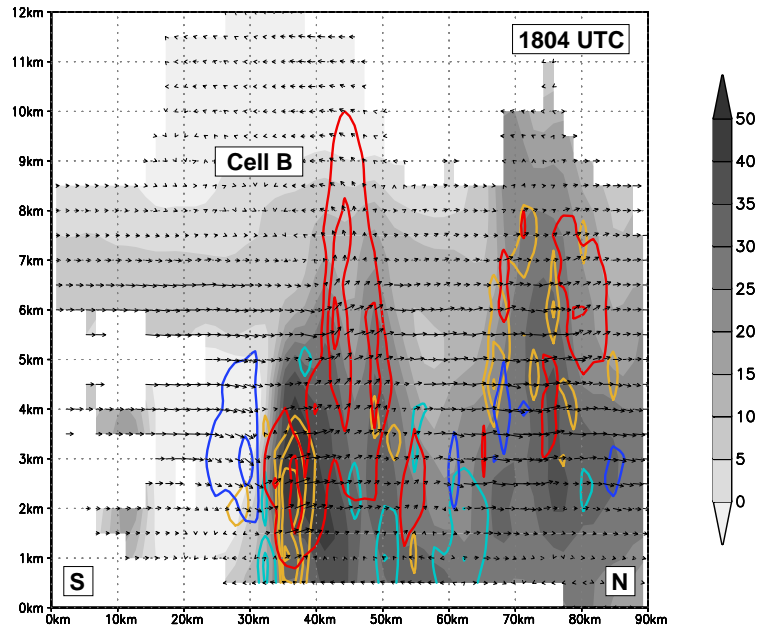
Figure 8: As in Figure 7, but for a north-south cross-section through Cell B. Wind vectors depict the vertical and cell-relative meridional flow.
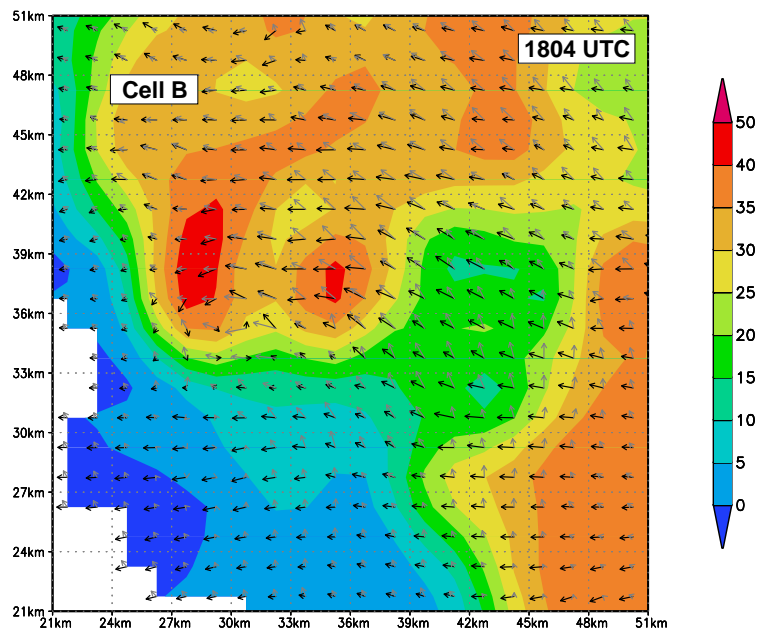
Figure 9: Horizontal vorticity vectors (gray), cell-relative wind vectors (black), and radar reflectivity (color shading) at 1.0 km altitude near Cell B at ~1804 UTC on 15 September 2004. Note the near-alignment of the vectors just to the east (the inflow) of the reflectivity maxima associated with the mesocyclonic updraft.
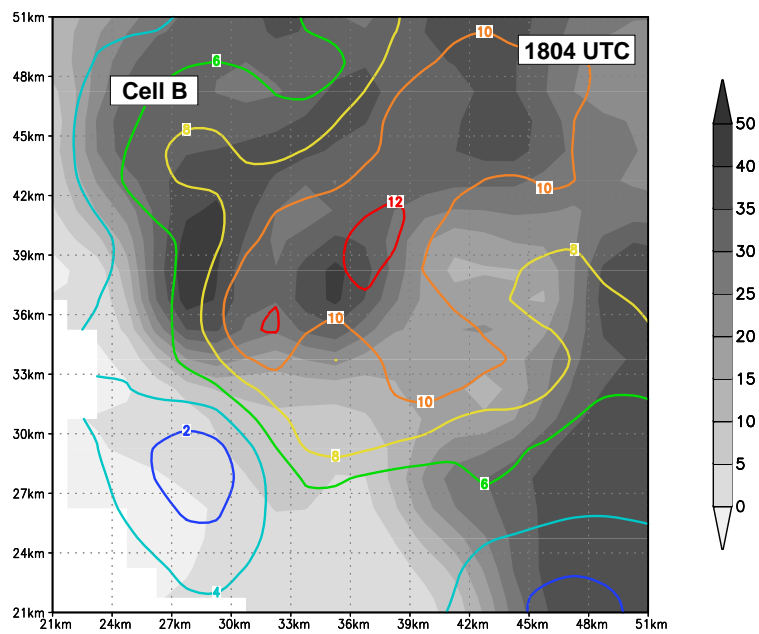

Figure 10: Horizontal vorticity magnitude (contours in 10^{-3} s^{-1}) and radar reflectivity (gray-scale shading) at 1.0 km altitude near Cell B.
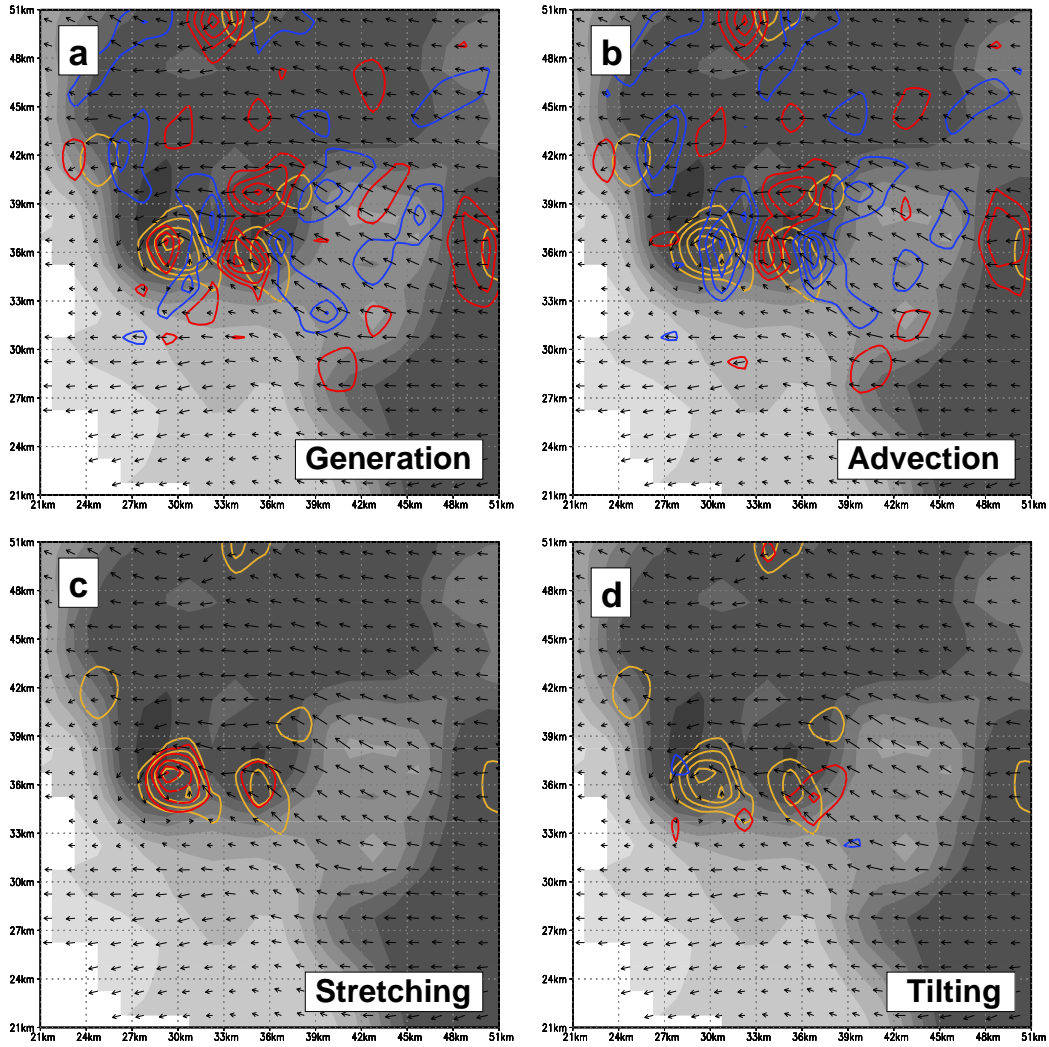
Figure 11: Distribution of the dual-Doppler derived (a) generation, (b) advection, (c) stretching, and (d) tilting terms of the vertical vorticity budget at 1.0 km altitude near Cell B at ∼1804 UTC on 15 September 2004. Red (blue) contours are positive (negative) contributions to vertical vorticity production. Contours of ±5, ±10, ±15, ±20, and ±25 x 10^{-6} s^{-2} are shown for each vorticity production term. Also shown are cyclonic vertical vorticity (orange contours at 2, 4, 6, and 8 x 10^{-3} s^{-1}), radar reflectivity (gray-scale shading), and cell-relative wind vectors.
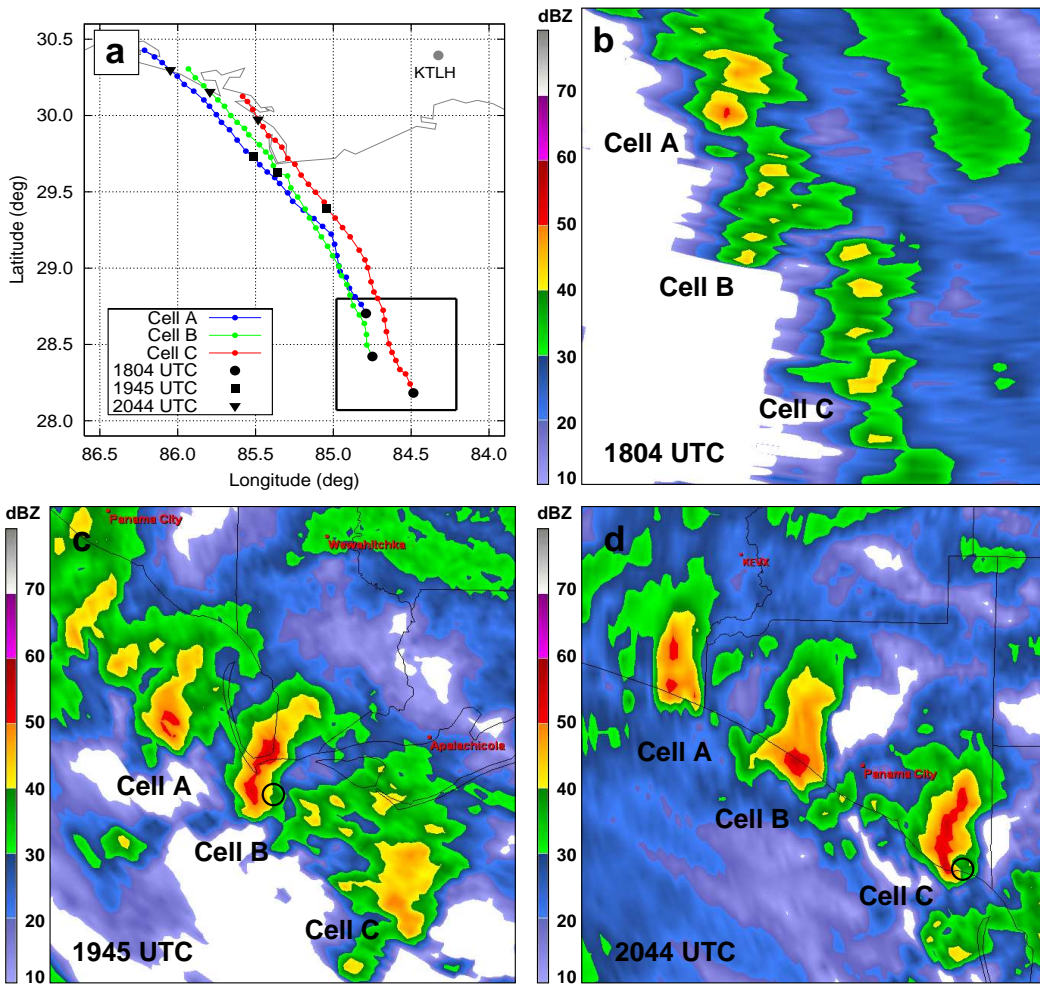
Figure 12: (a) Locations of Cells A, B, and C between 1800-2100 UTC on 15 September 2004 as determined from the Tallahassee (TLH) WSR-88D radar. Radar reflectivity at 0.5 deg elevation for the Cells A, B, C as viewed from TLH during (b) the dual-Doppler analysis at ∼1804 UTC, (c) the first mesocyclone detection (in Cell B) at ∼1945 UTC, and (d) the first reported tornado (from Cell C) at ∼2044 UTC. The black circulation markers denote radar-detected mesocyclones.